Regional Characteristics of the Northern Hemisphere Wintertime Circulation: A Comparison of the Simulation of a GFDL General Circulation Model with Observations

MAURICE L. BLACKMON

National Center for Atmospheric Research,[1] Boulder, CO 80307

NGAR-CHEUNG LAU

Geophysical Fluid Dynamics Program, Princeton University, Princeton, NJ 08540

(Manuscript received 29 May 1979, in final form 30 October 1979)

ABSTRACT

The hemispheric distributions of a selected set of temporal mean, variance and covariance statistics produced by a general circulation model developed at the Geophysical Fluid Dynamics Laboratory are compared with observations. The fields presented include 1) the seasonally averaged 300 mb geopotential height and zonal wind speed, sea level pressure and 500 mb vertical velocity; 2) the root-mean-squares of 500 and 1000 mb heights, and of 850 mb temperature; 3) the correlation coefficient between the 1000 and 500 mb heights, and 4) the horizontal and vertical transports of heat by transient eddies in the lower troposphere, and the horizontal eddy transports of momentum and potential vorticity near the tropopause. The partitioning of the variance of 500 mb height according to fluctuations of different temporal and spatial scales is examined. By making use of time filters which retain fluctuations with periods between 2.5 and 6 days, the characteristics of synoptic-scale disturbances appearing in the model are studied.

The regional contrasts of the observed wintertime circulation are simulated by the model. In particular, the transport properties of transient disturbances over the oceanic storm tracks and the locations of these centers of activity relative to the stationary flow field are reproduced. The agreement between model and observations substantiates some of our interpretations of the observed circulation presented in earlier works.

The model simulation differs from the observed atmosphere in the following aspects: 1) the amplitude of the simulated transient fluctuations in the upper troposphere is too weak; 2) the geographical distribution of the variance associated with low-frequency planetary-scale disturbances in the model bears little resemblance to the observed pattern; 3) the observed longitudinal variations of eddy activity in the middle and high latitudes are less evident in the model results; and 4) the simulated surface lows over Iceland and the Aleutians are too deep, so that the midlatitude westerlies over most of the Western Hemisphere are too strong, and the surface circulation over the North American continent is not realistic.

1. Introduction

During the past two decades, significant progress has been made in the development of three-dimensional general circulation models (GCM's) of the earth's atmosphere. The long-term integration of these numerical models, as reported, for example, by Kasahara and Washington (1971), Arakawa (1972), Manabe *et al.* (1974) and Somerville *et al.* (1974), has resulted in an abundance of simulated data. Diagnostic studies of these data sets have broadened our understanding of the earth's climate. Sensitivity experiments using these GCM's have produced interesting results concerning the effects on the atmospheric circulation of orography (Kasahara *et. al.*, 1973; Manabe and Terpstra, 1974), doubling of CO_2 concentration (Manabe and Wetherald, 1975) and sea surface temperature anomalies (Chervin *et al.*, 1976). In order to assess the usefulness of GCM's in the study of climate and climate change, it is necessary to examine the skill of these models in reproducing the essential features of the atmosphere in its present climate state. The evaluation of various aspects of model performance can be made by comparing general circulation statistics generated by the model with those compiled from actual observations.

Until now the basis for comparisons has been mostly confined to zonally averaged circulation statistics as well as the global distributions of time-mean fields such as temperature and geopotential height at selected levels (e.g., Gates, 1975), and space-time dependence of spectra and cospectra of atmospheric variables (e.g., Hayashi, 1974; Hayashi and Golder, 1977; Pratt, 1979). Relatively little at-

[1] The National Center for Atmospheric Research is sponsored by the National Science Foundation.

0022-4928/80/030497-18$08.50

tention has been devoted to assessing the ability of the models to simulate the observed geographical distributions of temporal variance and covariance statistics. The regional characteristics of these second-moment statistics provide valuable information on the properties of transient disturbances over the centers of enhanced wave activity and on various interactive processes between the transient and stationary components of the atmospheric circulation. It is hence obvious that the verification of model-generated variance and covariance statistics against observations on a regional basis should serve as a useful diagnostic tool in the analysis of model output.

The regional characteristics of the observed Northern Hemisphere wintertime circulation have been examined and presented in several publications in this journal. It was found that the temporal variability of the 500 mb geopotential height field, partitioned into different spatial scales and frequency bands, exhibits a strong geographical dependence (Blackmon, 1976). The fluctuations of geopotential heights and other selected atmospheric variables with synoptic time scales attain maximum amplitudes over the central oceans near 45°N latitude (Blackmon *et al.*, 1977). These centers of eddy activity coincide closely with the axes of the principal oceanic storm tracks, and the bear a definite relationship with the standing wave pattern. The transient disturbances over these regions are characterized by enhanced poleward and upward heat transports in the lower troposphere, and by convergence of momentum transports in the upper levels (Blackmon *et al.*, 1977; Lau, 1979a). By considering the eddy transports of heat and potential vorticity in both meridional and zonal directions, it was demonstrated that the vectorial distribution of these horizontal fluxes exhibit well-defined patterns relative to the time-averaged temperature and geopotential height fields (Lau and Wallace, 1979). The evidence presented in Lau (1979a) on the vertical phase structure of synoptic disturbances and the associated transport properties suggest that the migratory wave disturbances over the midlatitude oceans are characterized by well-defined life cycles, in the course of which they undergo significant structural changes. Blackmon *et al.* (1979) have noted that the vertical structure of geopotential height fluctuations with temporal frequencies ranging from synoptic to interannual time scales also exhibits striking geographical contrasts.

We believe that it should prove useful to compare the output of a GCM with the observed statistics presented in the studies mentioned above. The comparison between observations and the model within such a framework will identify the successes and deficiencies of the model in simulating the regional characteristics of the atmospheric circulations; and also serve as a consistency check on our interpretation of the Northern Hemisphere wintertime circulation, based on observations alone.

It has been noted in Blackmon (1976) and Blackmon *et al.* (1977) that a substantial component of variance and covariance statistics is attributable to low-frequency fluctuations. As a result of inadequate sampling of these slowly varying fluctuations over the course of a single season, these statistics exhibit strong interannual variability. As one compares the statistics derived from model data for a single winter season with observed data compiled from long-term climatological records, it is important to take this problem into account. In the present study, time filters are used to identify the fluctuations of different temporal scales, and special attention is devoted to the relatively more stable statistics of fluctuations with synoptic time scales.

This study is not intended to be a comprehensive documentation of the performance of a GCM. Only a selected set of the circulation statistics which reveal the essential properties of the transient disturbances and their relationship with the time-mean flow will be presented. The observational and model data sets for this study, and the procedures employed for analyzing these data, are described in Section 2. The geographical distributions of some seasonally averaged fields are compared in Section 3. Temporal variance statistics for different spatial and temporal scales are discussed in Section 4. The geographical variations in the vertical structure of geopotential height fluctuations are presented in Section 5. The transport characteristics of the transient disturbances are discussed in Section 6.

2. The data sets and analysis procedures

The observational results of this work are based on the twice-daily National Meteorological Center (NMC) analyses of geopotential height, temperature and wind fields at selected pressure levels, as well as the 6 h forecast fields of vertical velocity. These data records are maintained in the tape library of the National Center for Atmospheric Research. The operational analysis/forecast procedure at NMC and the numerical prediction models used to produce the forecast fields of vertical velocity are briefly summarized in Lau (1979a, Section 2). The analyses of the 500 mb geopotential height variance are based on the nine winters from 1963/64 through 1971/72. All other comparisons, except those involving vertical velocity fields, are made with observations for the 11-winter period from 1965/66 through 1975/76. Vertical velocity fields were available for the winters from 1964/65 through 1971/72 and from 1975/76 through 1976/77. The winter season is defined as extending from 15 November to 14 March (13 March in leap years).

The GCM which provided the history tapes for the present study was developed at the Geophysical Fluid Dynamics Laboratory (GFDL) by Manabe and his co-workers to investigate the seasonal variation of the global circulation. The tropical circulation simulated by this model has been described by Manabe *et al.* (1974) and Hahn and Manabe (1975). The climatology and hydrological cycle of the model have been presented by Manabe and Holloway (1975). Space-time spectral analyses of tropical and midlatitude disturbances appearing in the model have been performed by Hayashi (1974) and Hayashi and Golder (1977).

The model uses a modified version of the horizontal grid system designed by Kurihara and Holloway (1967), so that a uniform resolution of ~265 km is achieved. The effects of mountains are treated in the model, using a sigma coordinate system consisting of 11 layers. The physical processes incorporated in the model include prescribed seasonal variation of solar radiation and sea surface temperature, radiative heating and cooling (Manabe and Wetherald, 1967), moist convective adjustment (Manabe *et al.*, 1965) and a hydrological cycle (Manabe, 1969). The surface temperature over land is determined by satisfying the constraint that no heat is stored in the ground. The model data records used in the present study consist of the daily fields of geopotential height, temperature, and horizontal and vertical velocity for a single 120-day period beginning 15 November. The daily values at all grid points were smoothed by retaining the first 20 zonal wavenumbers in a Fourier expansion.

The filtering procedure for retaining the low-frequency (periods $10 \leq T \leq 90$ days) and medium-frequency (periods $2.5 \leq T \leq 6$ days) fluctuations in the twice-daily NMC data was described in Blackmon (1976). The corresponding low-pass and bandpass filter coefficients are tabulated therein. Since the GCM data are available at daily intervals, new low-pass and bandpass filters with 21 points each were developed. The filter coefficients, as defined in Blackmon [1976, Eq. (15)], are given in Table 1. These filters have frequency responses nearly identical to the filters used for the observations, so that no conclusions in this paper can be attributed to differences in the filters used.

The 500 mb height fields were expanded in a series of spherical harmonics, in the manner described by Blackmon (1976). Three regimes in the two-dimensional wavenumber space were defined as follows:

$$\text{Regime I} \begin{cases} 0 \leq n \leq 6 \\ 0 \leq m \leq n \end{cases}$$

$$\text{Regime II} \begin{cases} 7 \leq n \leq 12 \\ 0 \leq m \leq n \end{cases}$$

TABLE 1. Values of the coefficients for the low-pass and bandpass 21-point filters discussed in the text.

Coefficients	Filters	
	Low-pass	Bandpass
a_0	0.2119623984	0.4522054510
a_1	0.1974416342	−0.0728693709
a_2	0.1576890490	−0.2885051308
a_3	0.1028784073	0.0973270826
a_4	0.0462514755	0.0395130908
a_5	0.0	0.0283273699
a_6	−0.0281981813	0.0331625327
a_7	−0.0368362395	−0.0708879974
a_8	−0.0300256308	−0.0022652475
a_9	−0.0151817136	0.0030189695
a_{10}	0.0	0.0070759754

$$\text{Regime III} \begin{cases} 13 \leq n \leq 18 \\ 0 \leq m \leq n\,. \end{cases}$$

Here m is the zonal wavenumber and n the two-dimensional wavenumber. Waves in Regimes I, II and III will be referred to as planetary-scale waves, synoptic-scale waves and short waves, respectively. For a more detailed discussion on the general representation of spatial scales in the (n,m) space, and on the particular truncation procedure used here, the reader is referred to the paper by Blackmon (1976, Section 2).

3. Structure of the seasonally averaged circulation

The distribution of the time-averaged geopotential height field is shown in Fig. 1a for the atmosphere at 300 mb and in Fig. 1b for the GFDL model atmosphere at 315 mb. Superimposed on these patterns are dashed contours depicting regions with strong zonal wind. The axes of the major stationary troughs are represented by dotted lines. Comparison between these two patterns indicates that the horizontal phase of the observed stationary wave is simulated by the model. There is also good agreement in the location of the wintertime jet stream over the western Pacific. However, the axis of the simulated jet stream over the northern Atlantic is shifted poleward and eastward relative to that observed in the atmosphere. The maximum wind speeds of the jet streams in the model are weaker than those observed by ~8 m s^{-1}.

In Fig. 2 we show the distribution of the time-averaged sea level pressure field for the atmosphere (Fig. 2a) and the model (Fig. 2b). The location of the lows over Iceland and the Aleutians, as well as that of the highs over central Asia and the eastern portion of the subtropical oceans, are reproduced by the model. The major lows are deeper than those observed by 10–20 mb; so that the simulated pressure gradients over the midlatitude oceans are too strong.

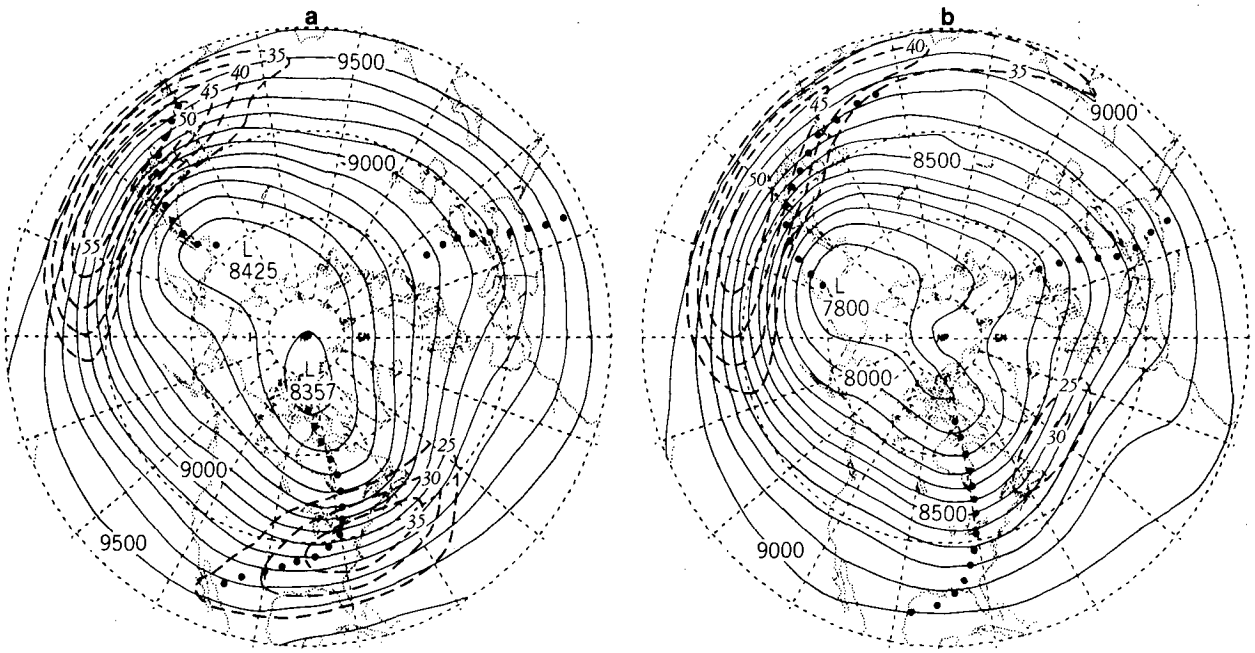

FIG. 1. Distributions of the time-mean geopotential height field (solid contours, interval 100 m) and zonal wind field (dashed contours, interval 5 m s^{-1}) for (a) observations at 300 mb and (b) the model simulation at 315 mb. The axes of the principal stationary troughs are depicted by dotted lines. The figures in this paper are all displayed on polar stereographic projections. The meridians and latitude circles are drawn at an interval of 20°, the outermost latitude circle represents 20°N.

The belt of surface westerlies in the model extends all the way from the western Pacific to western Europe; whereas the observed westerlies are confined to regions lying over the two major oceans. This leads to a rather unrealistic surface wind circulation over the North American continent in the model.

The distribution of vertical velocity in pressure coordinates at 500 mb is shown in Fig. 3a as obtained from the 6 h forecast fields produced by the NMC

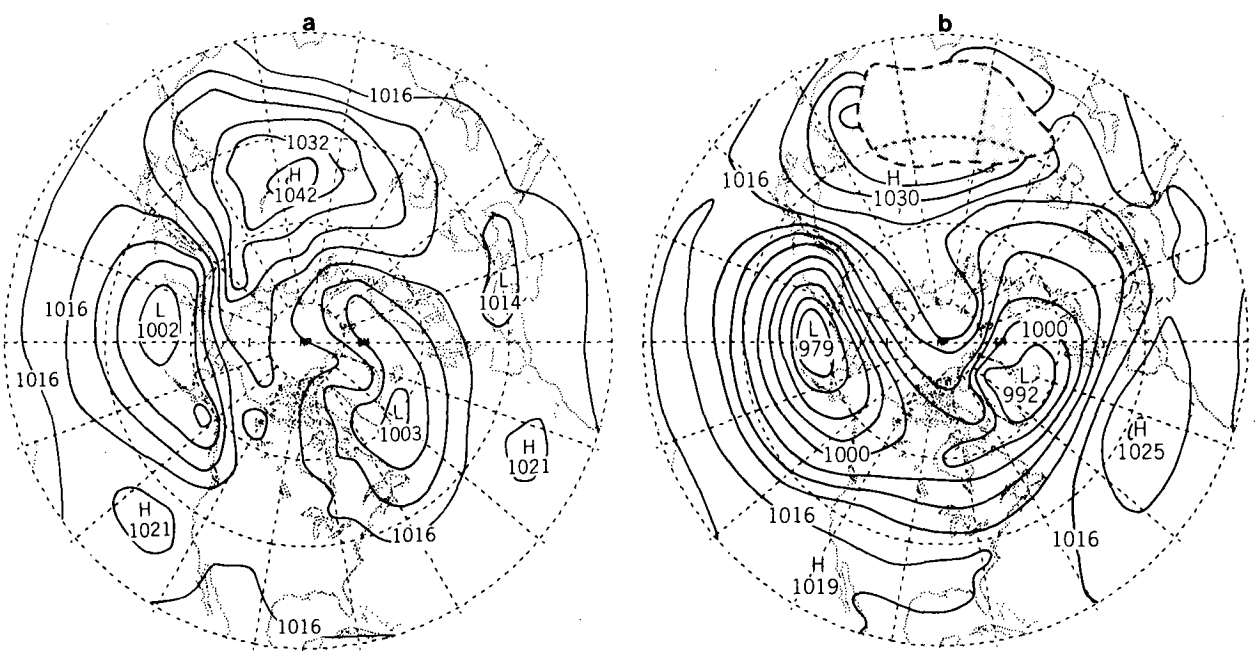

FIG. 2. Distribution of the time-mean sea level pressure field for (a) observations and (b) the model simulation. Contour interval 4 mb.

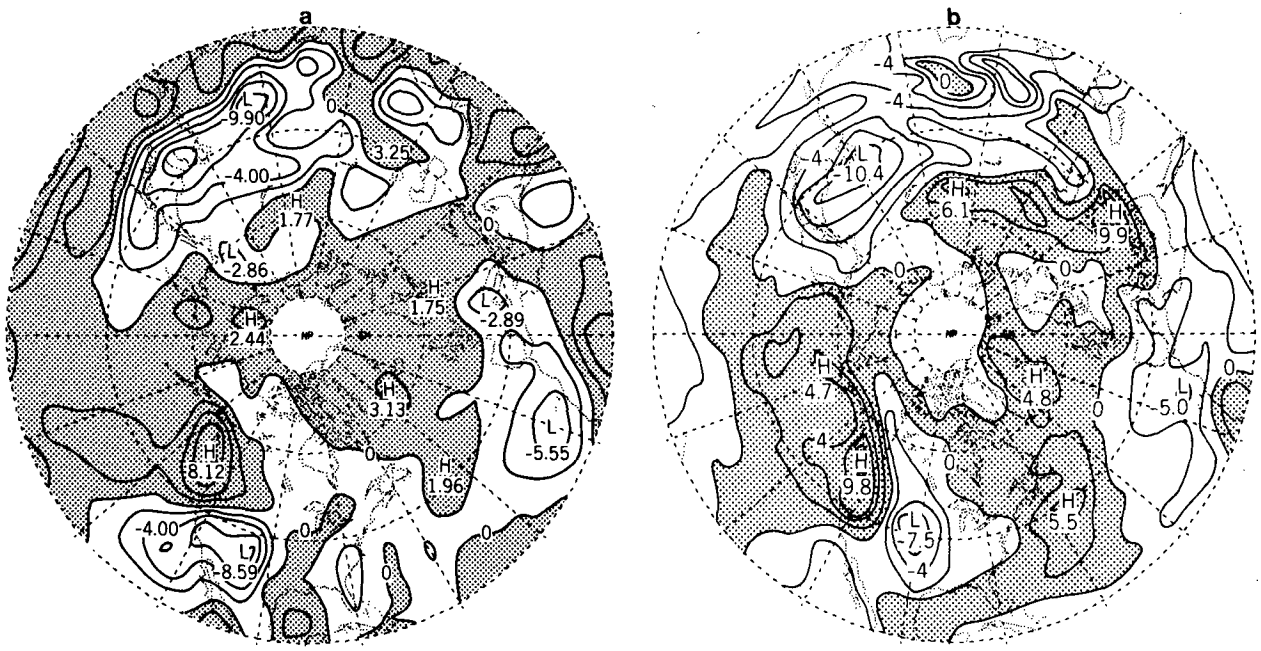

FIG. 3. Distribution of the time-mean vertical velocity at 500 mb, as computed using (a) NMC data and (b) GFDL model data. Contour interval 2×10^{-4} mb s^{-1}.

numerical prediction models, and in Fig. 3b from the data generated by the GFDL GCM. These two patterns are seen to display several common features which are closely related to the underlying topography and the sea level pressure pattern (Fig. 2):

- Rising motion on the windward side of the Canadian Rockies.
- Sinking motion on the leeward side of the Rockies and the Tibetan Plateau.
- Large-scale ascent over the northern Pacific and northern Atlantic, which correspond geographically to low-pressure centers at sea level.
- Large-scale subsidence over the eastern portion of the subtropical oceans, where high-pressure centers are located at sea level.

There are also notable differences between the two distributions:

1) The NMC data indicate that the subtropical western Pacific and central Sahara are characterized by rising motion; the GFDL model data indicate that sinking motion prevails over these regions. In view of the proximity of these subtropical regions to the boundary of the integration domain for the NMC prediction models, and of the paucity of actual observations over the same areas, the NMC forecast fields of vertical motion in the low latitudes should be examined with caution. As further evidence of the uncertainties of the NMC vertical velocity data over the subtropics, we note that, contrary to our knowledge of the zonally averaged meridional circulation, the NMC data give prevalent rising motion along the 20°N latitude circle. In the case of the Sahara, the vertical velocities produced by the GCM are probably more realistic than those derived from the NMC forecast fields.

2) In the GFDL model atmosphere, the oceanic area off the eastern seaboard of the United States is dominated by rising motion, whereas the NMC data suggest that this region is characterized by subsidence.

Since the absolute magnitude of the vertical motion generally decreases with height above 500 mb, one would expect mean rising (sinking) motion at 500 mb to correspond with mean divergence (convergence) in the upper troposphere. The time-averaged budget of absolute vorticity requires that this divergence field must be balanced locally by vorticity advection by the stationary flow and convergence of vorticity transports by the transient eddies [e.g., see Lau, 1979b, Eq. (1)]. The distributions of the time-averaged streamfunction $\bar{\psi}$ (solid contours) and absolute vorticity $\bar{\zeta} + f$ (dashed contours) are displayed in Fig. 4, for the atmosphere at 300 mb (Fig. 4a) and the GFDL model at 315 mb (Fig. 4b). Comparison between Figs. 3 and 4 reveals that, for both data sets, the principal centers of divergence (convergence) in the upper troposphere coincide with positive (negative) advection of absolute vorticity by the stationary flow. It is particularly worth noting that, for the NMC data, the rising motion over the Sahara is associated with positive vorticity advection by the stationary flow at 300 mb; whereas

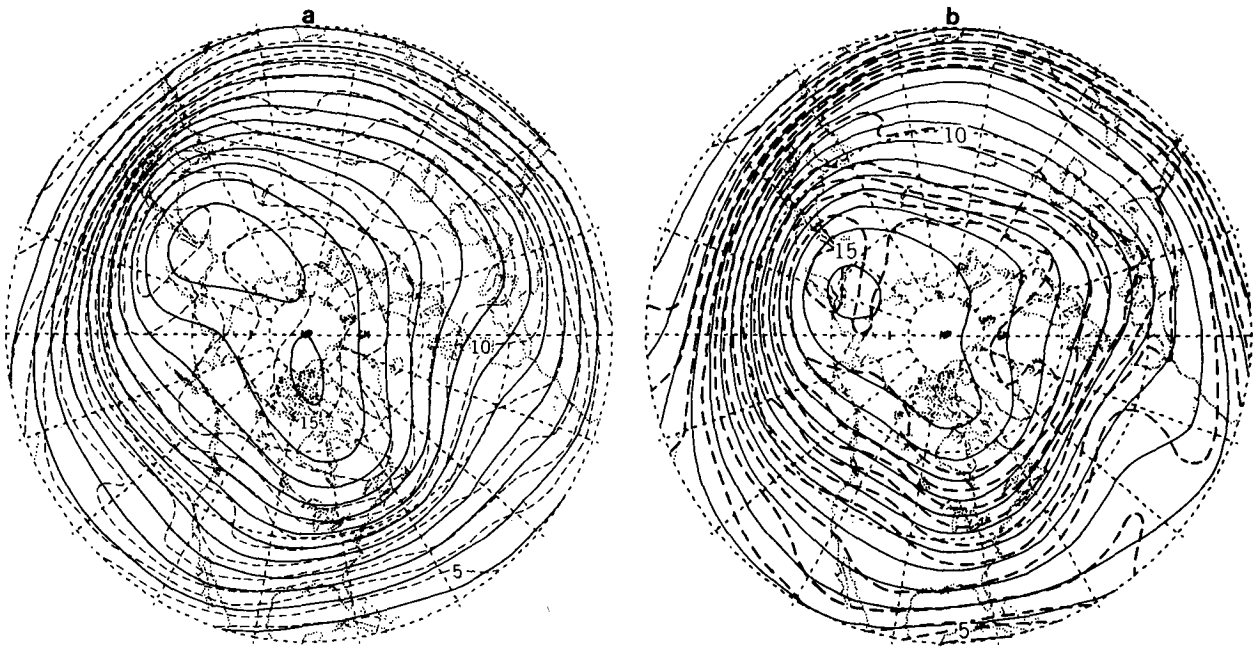

FIG. 4. Distributions of the time-mean streamfunction (solid contours, interval 10^7 m^2 s^{-1}) and absolute vorticity (dashed contour, interval 10^{-5} s^{-1}) for (a) observations at 300 mb and (b) the model simulation at 315 mb.

the GCM simulation indicates that the prevalent sinking motion over the same region is associated with negative vorticity advection.

A comparison of the mean 850 mb temperature field is included in Section 6, together with a discussion of its relationship with the eddy sensible heat flux.

4. Temporal variance statistics

In Fig. 5 we show the root-mean-square (rms) of the 500 mb height for (a) observations and (b) the model. The geographical locations of the three observed maxima over the northern Pacific, the northern Atlantic and north-central Asia are reproduced

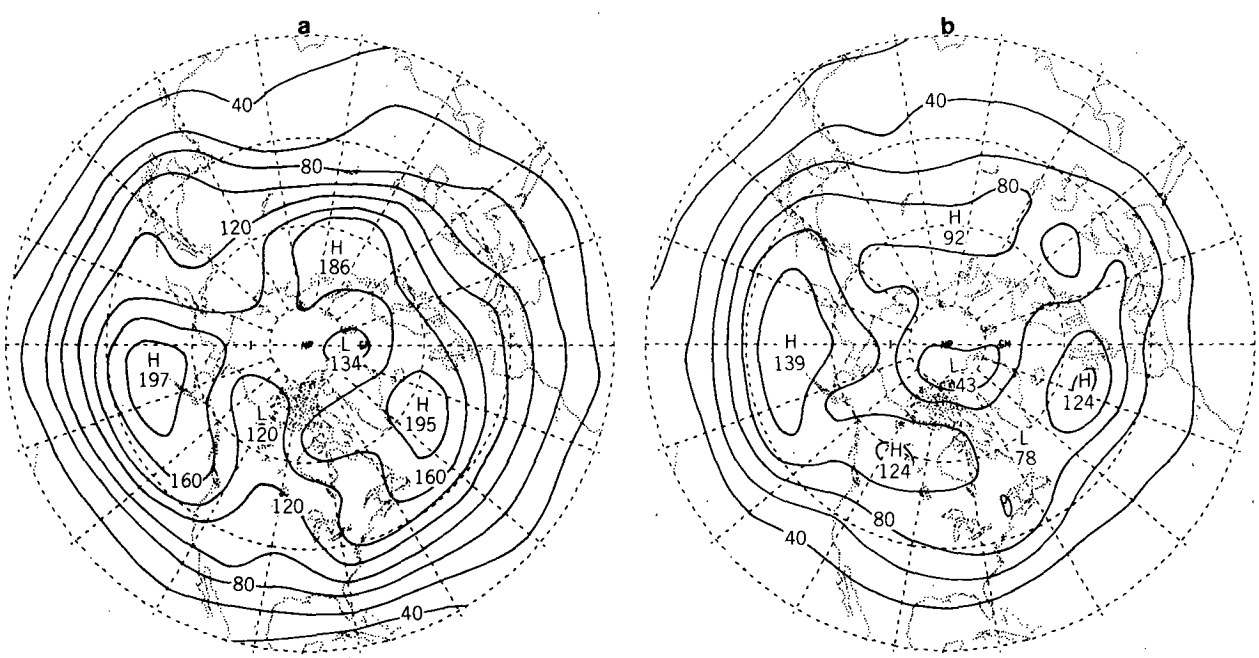

FIG. 5. Distribution of the root-mean-square (rms) of the 500 mb height for (a) observations and (b) model simulation. Contour interval 20 m.

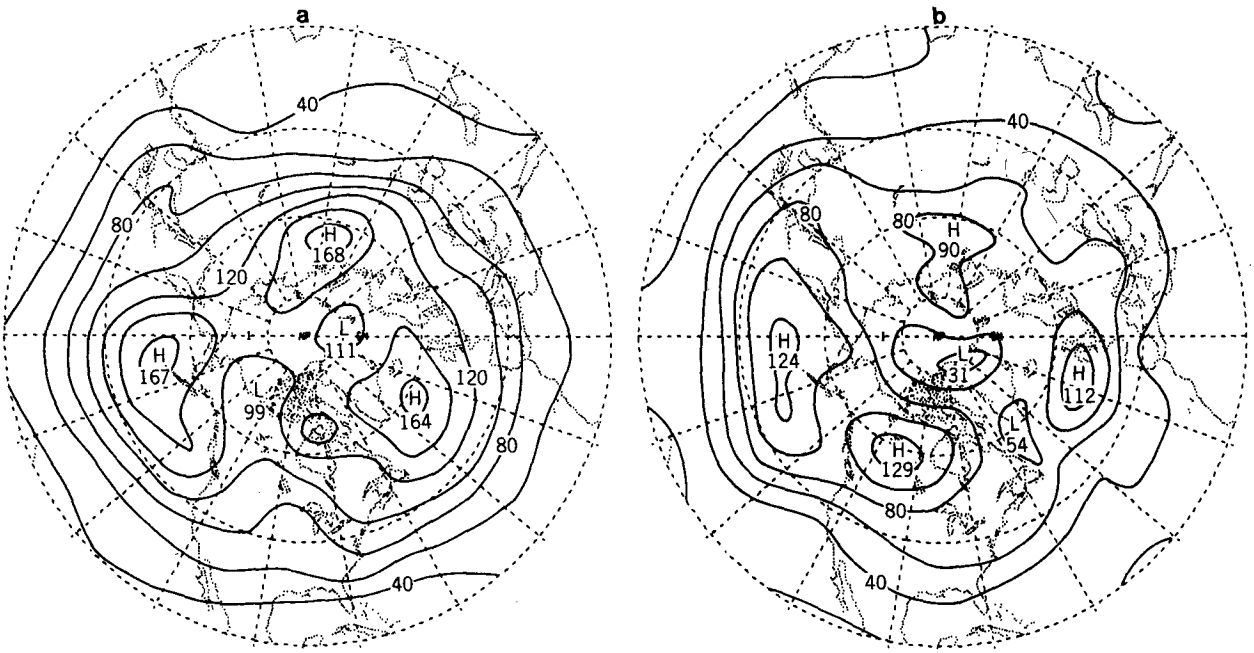

FIG. 6. Distribution of the low-pass filtered rms of the 500 mb height for (a) observations and (b) model simulation. Contour interval 20 m.

by the model. The magnitudes of the geopotential height fluctuations in the model are ~60% of those observed. The model produces a fourth maximum over western Canada, with an amplitude which is comparable to those associated with centers over the northern oceans. There is no indication of this "Canadian center" in the observed pattern. In two winters of the data set, 1964/65 and 1969/70, the Pacific center is characterized by the presence of a secondary maximum which extends from 120 to 140°W, some 10–20° west of the "Canadian center" simulated by the model. In some winters, the observed Atlantic center is displaced considerably west of its mean position. However, it is never displaced beyond Hudson Bay. We therefore conclude that the "Canadian center" simulated by the model is probably unrealistic and is beyond the limits of observed interannual variability. The magnitudes of the observed fluctuations exhibit strong longitudinal variations along the zonal belt between 40 and 70°N latitudes (Fig. 5a). In association with the enhanced eddy amplitudes over northwestern Canada and eastern Siberia, the longitudinal contrast in eddy activity is much less evident in the model.

In Fig. 6 we show the low-pass filtered rms field of 500 mb heights for (a) observations and (b) the model. The similarity between the observed unfiltered field (Fig. 5a), and the observed low-pass filtered field (Fig. 6a), was noted by Blackmon (1976). The resemblance between the corresponding fields for the model (Figs. 5b and 6b) indicates that, in agreement with observations, the low-frequency fluctuations in the model account for a substantial fraction of the total variance. The amplitude of low-frequency fluctuations in the model is generally weaker than those in the observed atmosphere. This is consistent with the spectral results presented by Hayashi and Golder (1977, Fig. 4.4) and Pratt (1979, Fig. 3b).

Fig. 7a shows the observed low-pass filtered rms of the 500 mb height for waves in Regime I, $0 \leq n \leq 6$, and Fig. 7b the corresponding model simulation. It is seen that this pair of patterns bears little resemblance to each other. The agreement between the model and observations is not too close for the following reasons:

1) As a result of insufficient sampling of low-frequency, planetary-scale fluctuations over an individual season, the low-pass statistics for waves in Regime I are highly variable from one winter to another. Even though certain characteristics of the model simulation shown in Fig. 7b are present in the observed patterns for particular winters (not shown), such similarities are much less evident when the model result is compared with the observed long-term average shown in Fig. 7a.

2) Comparing Figs. 4a, 4b and 4c in Blackmon (1976), we see that the observed low-pass field has important contributions from both planetary-scale (Regime I) waves and synoptic-scale (Regime II) waves. Comparing Figs. 6b and 7b here, we see that planetary-scale (Regime I) waves in the model totally dominate the low-frequency field. The contribution

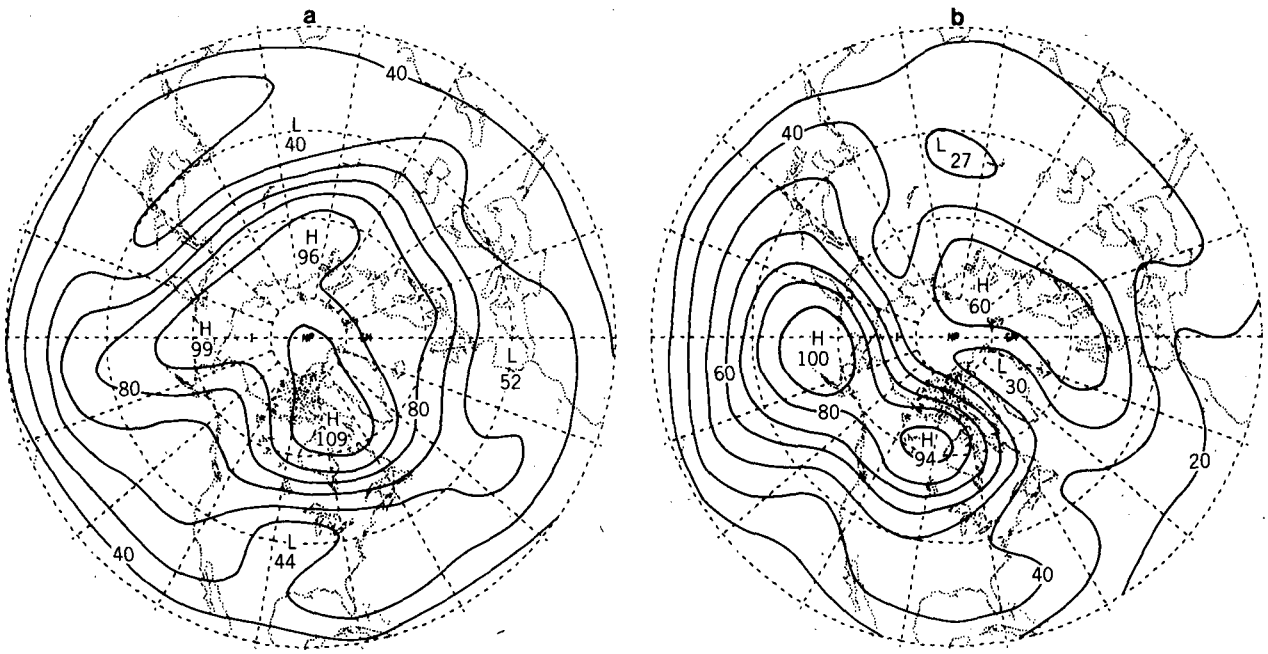

FIG. 7. Distribution of the low-pass filtered rms of the 500 mb height for planetary-scale waves in Regime I for (a) observations and (b) model simulation. Contour interval 10 m.

to low-pass variance from synoptic-scale (Regime II) waves in the model (not shown) is weaker than the contribution from planetary-scale waves by approximately a factor of 2.

Comparison between the model results in Figs. 5b, 6b and 7b indicates that low-frequency, planetary-scale fluctuations are largely responsible for the enhanced geopotential height variability over northern Canada. This is consistent with the analysis of Hayashi and Golder (1977, Fig. 6.5), who noted that this same region corresponds to a maximum in the amplitude of geopotential height fluctuations with zonal wavenumbers 0–3 and periods of 20–30 days.

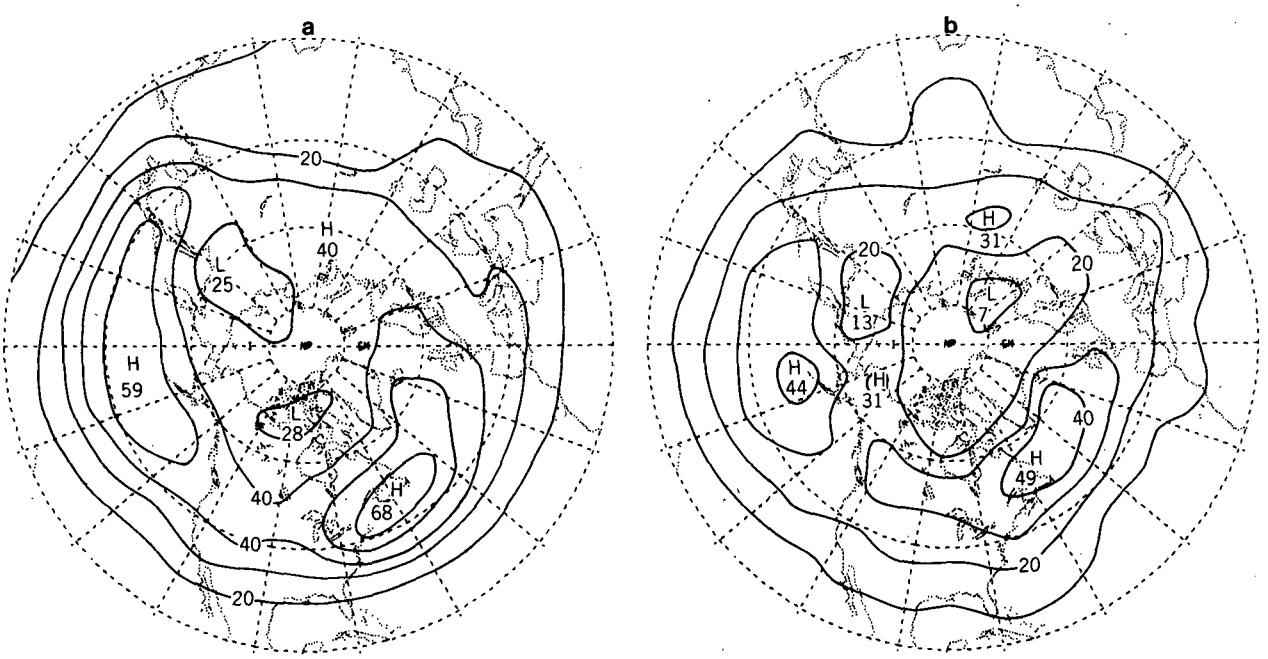

FIG. 8. Distribution of the bandpass filtered rms of the 500 mb height for (a) observations and (b) model simulation. Contour interval 10 m.

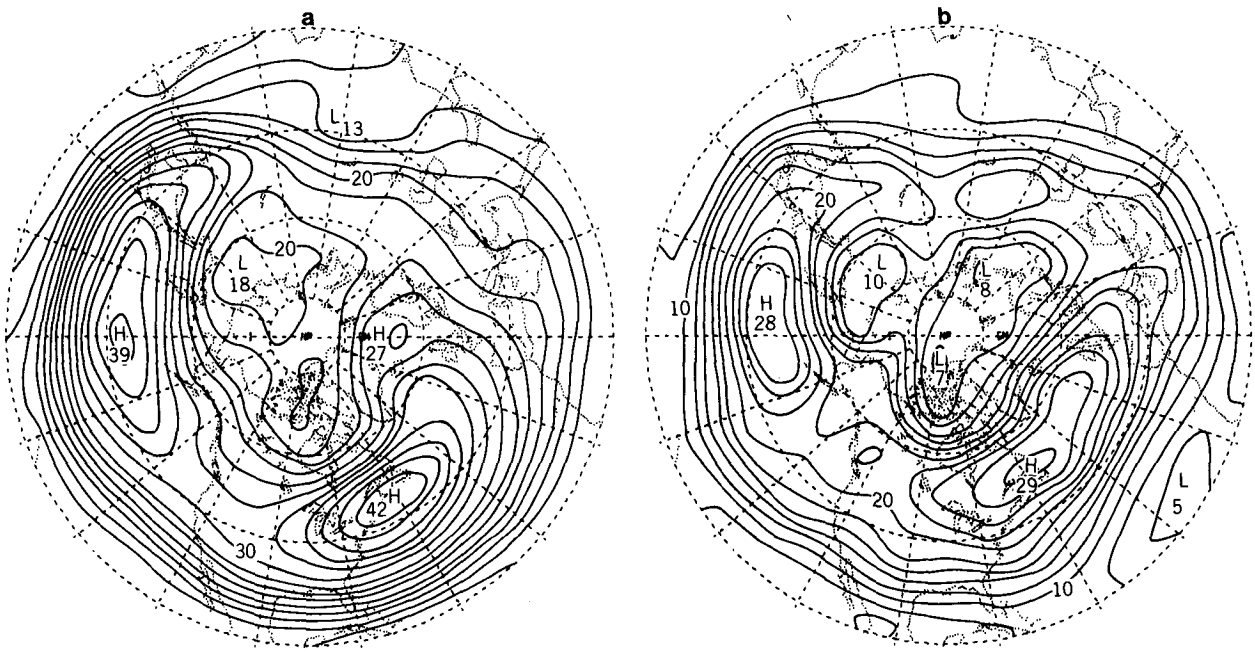

FIG. 9. Distribution of the bandpass filtered rms of the 500 mb height for synoptic-scale waves in Regime II for (a) observations and (b) model simulation. Contour interval 2 m.

In Fig. 8 we show the bandpass filtered rms of the 500 mb height for observations (Fig. 8a) and the model (Fig. 8b). As discussed in Blackmon (1976) and Blackmon *et al.* (1977), the elongated maxima near 40°N which extend from the eastern continents across the oceans correspond to the major "storm tracks" of the Northern Hemisphere. Comparison between Fig. 1 and Fig. 8 indicates that for both observations and the model, these oceanic storm tracks are located slightly poleward and downstream of the principal wintertime jet streams. In association with the poleward and eastward displacement of the modeled Atlantic jet stream relative to its observed location, we note a corresponding shift in the position of the storm track axis over this region. The maximum over north-central Asia (80°E, 60°N) and the regions of suppressed activity over northeastern Asia and north-central Canada are simulated by the model. The amplitude of the bandpass fluctuations in the model is ~75% of the corresponding observed results. Comparing the model statistics with those for individual winters in the observational data set, we conclude that the amplitude of bandpass fluctuations at 500 mb in the model is relatively weaker, even if interannual variability is taken into account.

Although the location and intensity of the storm tracks vary from year to year, the observed bandpass fields for individual winters in our observational data set are substantially less variable than either the unfiltered fields or the low-pass filtered fields. Comparison of the model result in Fig. 8b with the corresponding observed patterns for individual winters indicates that the slight displacements of the major features produced by the model relative to the long-term observed pattern are probably within reasonable limits of observed interannual variability.

In Fig. 9 we show the contribution to the bandpass filtered rms of the 500 mb heights by waves in Regime II ($7 \leq n \leq 12$) for (a) observations and (b) the model. Analysis of the observational data indicates that waves in Regimes II and III have rms maxima approximately 65 and 45%, respectively, of the total rms field (see Blackmon, 1976, Figs. 5c and 5d). Comparison between Figs. 8b and 9b indicates that this partitioning of bandpass variance between synoptic-scale and short waves is reproduced by the model.

In Fig. 10 we compare the rms of geopotential height for (a) observations at 1000 mb and (b) the model at 990 mb. For both observations and the model there is a close correspondence between the pattern of geopotential height variance near sea level and the corresponding field at 500 mb, shown in Fig. 5. Over the northern Pacific, the amplitude of height fluctuations in the model is in closer agreement with observations at sea level than at 500 mb.

In Fig. 11 we show the bandpass filtered rms of (a) the observed 1000 mb height and (b) the 990 mb height for the model. There is a good correspondence between the model and observations. As noted in Blackmon *et al.* (1977), the observed fluctuations near sea level are enhanced along the east side of the major mountain ranges, particularly in the bandpass

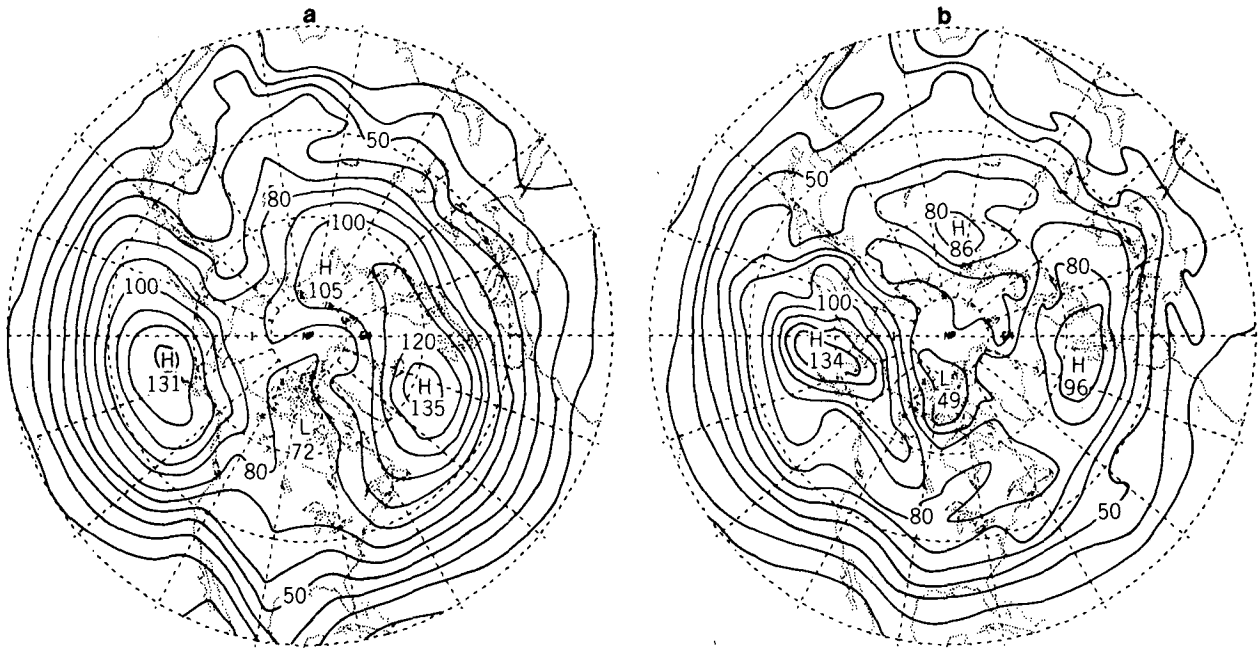

FIG. 10. Distribution of the rms of geopotential height for (a) observations at 1000 mb and (b) model simulation at 990 mb. Contour interval 10 m.

portion of the spectrum. This is most evident east of the Rockies and the Tibetan Plateau. The model also shows such enhancements, particularly east of the Rockies. Another notable feature in the observed pattern is the region of reduced bandpass activity over northeastern Asia. There is some indication of this feature near 40°N latitude in the model result.

As discussed in Blackmon *et al.* (1977), the large-scale patterns of geopotential height variance at 1000, 500 and 300 mb are all qualitatively similar. The vertical profiles of the maxima in the bandpass

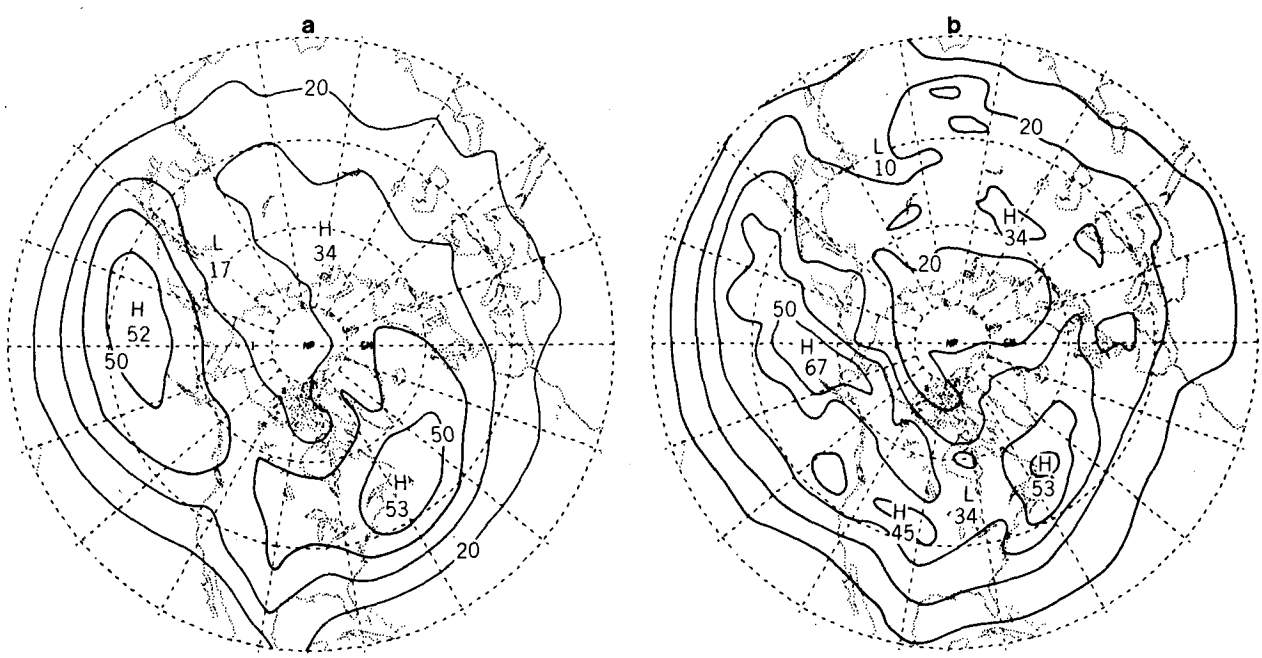

FIG. 11. Distribution of the bandpass filtered rms of geopotential height for (a) observations at 1000 mb and (b) model simulation at 990 mb. Contour interval 10 m.

filtered rms of geopotential height over the oceanic storm tracks are compared in Table 2. As noted in Lau (1978), the observed variance exhibits a relative minimum at 850 mb. There is some indication of this feature over the Atlantic in the model simulation. The location of this minimum over the Pacific occurs near 500 mb in the model. The observed variability increases with height in the middle and upper troposphere, reaching a maximum at 300 mb. The amplitude of the observed geopotential height fluctuations increases by a factor of about 1.7 between the 1000 and 300 mb levels; the corresponding values for the model are 1.3 (Pacific) and 0.9 (Atlantic).

The bandpass filtered rms of the observed 850 mb temperature is shown in Fig. 12a and the 835 mb temperature for the model in Fig. 12b. The geographical location and magnitude of the maxima over the oceanic storm tracks are reproduced by the model. The region of low variability along the west coast of North America is less evident in the model result.

In Table 2 we also compare the values of the maxima in the bandpass filtered rms of temperature over the major storm tracks for various levels. It is seen that the simulated temperature fluctuations in the upper troposphere over the Atlantic are relatively weak in comparison with observations.

TABLE 2. The vertical profiles of the maxima in the rms bandpass filtered geopotential height (top) and temperature (bottom) over the Pacific and Atlantic storm tracks, for the atmosphere (left) and model (right).

	Atmosphere		Model	
	Atlantic	Pacific	Atlantic	Pacific
Bandpass geopotential height $(\overline{z'^2})^{1/2}$, units m				
300 mb	90	81	71	63
500 mb	68	59	49	44
850 mb	46	45	42	58
1000 mb	53	52	53	67
	Atlantic	Pacific	Atlantic	Pacific
Bandpass temperature $(\overline{T'^2})^{1/2}$, units °C				
300 mb	2.0	2.1	1.3	1.9
500 mb	3.2	3.0	2.6	3.1
850 mb	3.6	2.8	3.6	3.0

5. Vertical structure of geopotential height fluctuations

On the basis of a detailed analysis of an observational data set covering 15 years. Blackmon *et al.* (1979) noted that the vertical structure of temporal fluctuations in the geopotential height field exhibits large regional contrasts. In particular, it was found that the hemispheric distribution of the correlation coefficient between 1000 and 500 mb heights is characterized by strong geographical variability. In order to evaluate the ability of the model to reproduce the gross features of these regional variations, the distributions of the correlation coefficient between 1000 and 500 mb heights for the atmosphere and the model are compared in Fig. 13. These patterns are obtained using unfiltered twice-daily obser-

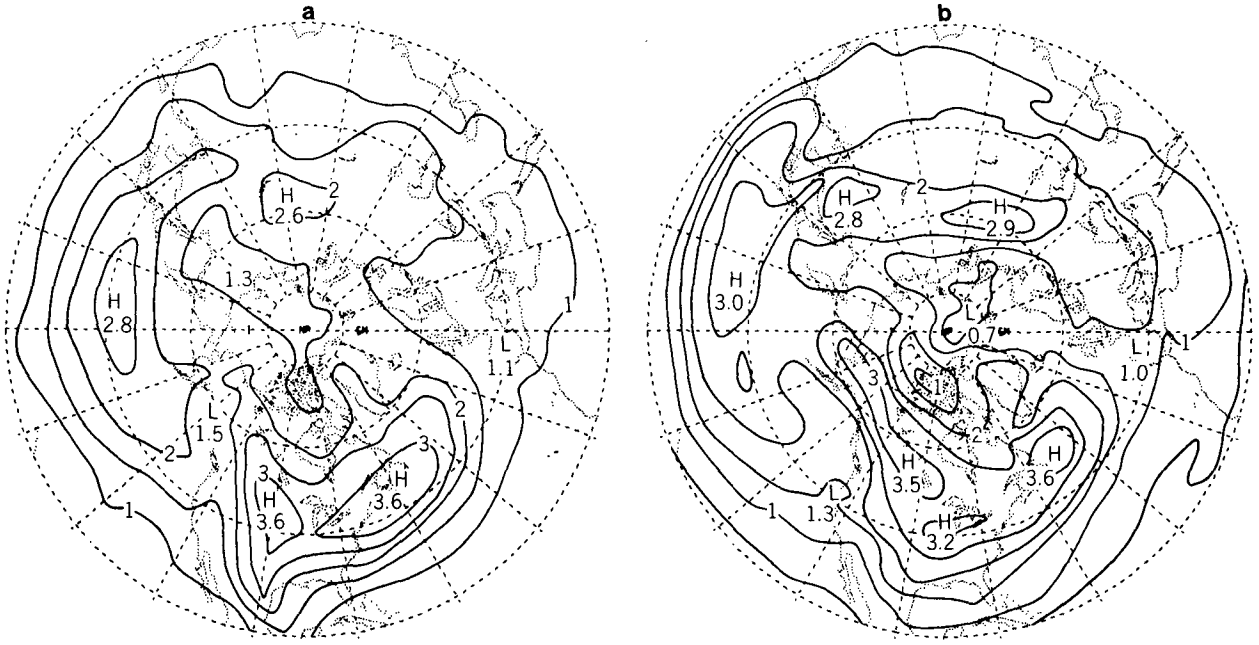

FIG. 12. Distribution of the bandpass filtered rms of temperature for (a) observations at 850 mb and (b) model simulation at 835 mb. Contour interval 0.5°C.

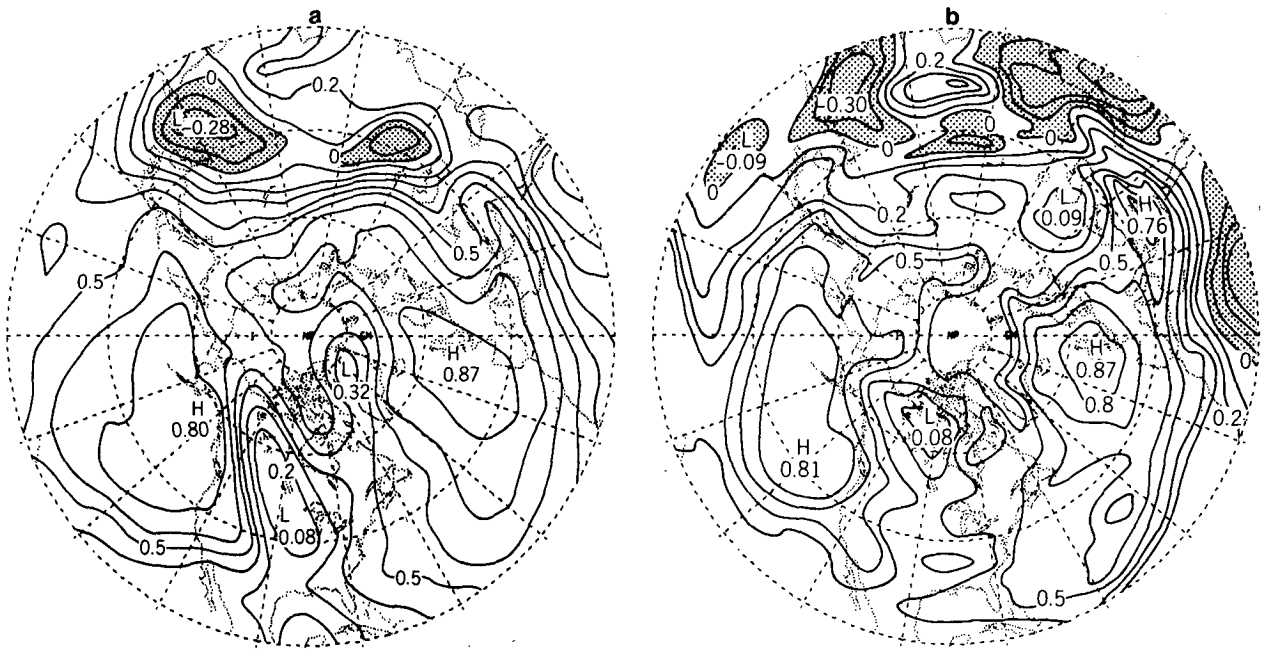

FIG. 13. Correlation coefficient between (a) 1000 and 500 mb heights for observations and (b) 990 and 500 mb heights for model simulation. Contour interval 0.1.

vations (Fig. 13a) and daily model data (Fig. 13b). It is seen that they exhibit a strong resemblance to each other over most regions of the Northern Hemisphere. The eastern portion of the midlatitude oceans and the Mediterranean are characterized by high positive correlations, which suggests that the transient fluctuations over these regions possess a barotropic structure. On the other hand, the correlations over the interiors of the North American and Eurasian continents are generally low or negative, indicating that the vertical structure of the disturbances over these locations is relatively more baroclinic.

The distribution of the correlation coefficient between 1000 and 500 mb heights using bandpass filtered model data (not shown) is less organized than the corresponding pattern using unfiltered data (shown in Fig. 13b). However, the gross features of the bandpass result are in agreement with observations (Blackmon *et al.*, 1979, Fig. 3b), with gradually increasing correlation coefficients as one moves eastward from the oceanic storm tracks to the west coasts of North America and Europe.

6. Transports by transient eddies

a. Heat transport

In Fig. 14 we show the distribution of meridional heat transport by transient eddies, as computed using bandpass filtered data for (a) the atmosphere at 850 mb and (b) the GFDL model atmosphere at 835 mb. It is seen that the magnitude and location of the maxima in poleward heat flux over the oceanic storm tracks are reproduced by the model. The much weakened heat transports over the western United States and western Europe are also evident in both patterns.

The distribution of horizontal heat transport by transient eddies is displayed in Fig. 15 in a vectorial format, using unfiltered data for the atmosphere at 850 mb (Fig. 15a) and the GFDL model atmosphere at 835 mb (Fig. 15b). The vector field of horizontal eddy heat transports $\mathbf{F}(T) \equiv \overline{u'T'}\mathbf{i} + \overline{v'T'}\mathbf{j}$ is depicted by arrows centered at selected grid points. Here $\mathbf{i}$ and $\mathbf{j}$ are the unit vectors in the zonal and meridional directions, respectively; the overbars denote time averages and primes denote deviations from time averages. The length and orientation of each arrow indicate the flux intensity and flux direction, respectively. The corresponding distribution of time-averaged temperature (contour lines) is superimposed on these patterns. The eddy heat transports in both the observed and model atmospheres are directed down the local horizontal temperature gradient. These fluxes tend to converge toward northeastern Asia and northeastern Canada, where they act to destroy the negative anomalies in the stationary temperature field. Since the departure from zonal symmetry of the time-averaged temperature field is a measure of the available potential energy of the standing waves, the heat transports by transient eddies in both the atmosphere and the

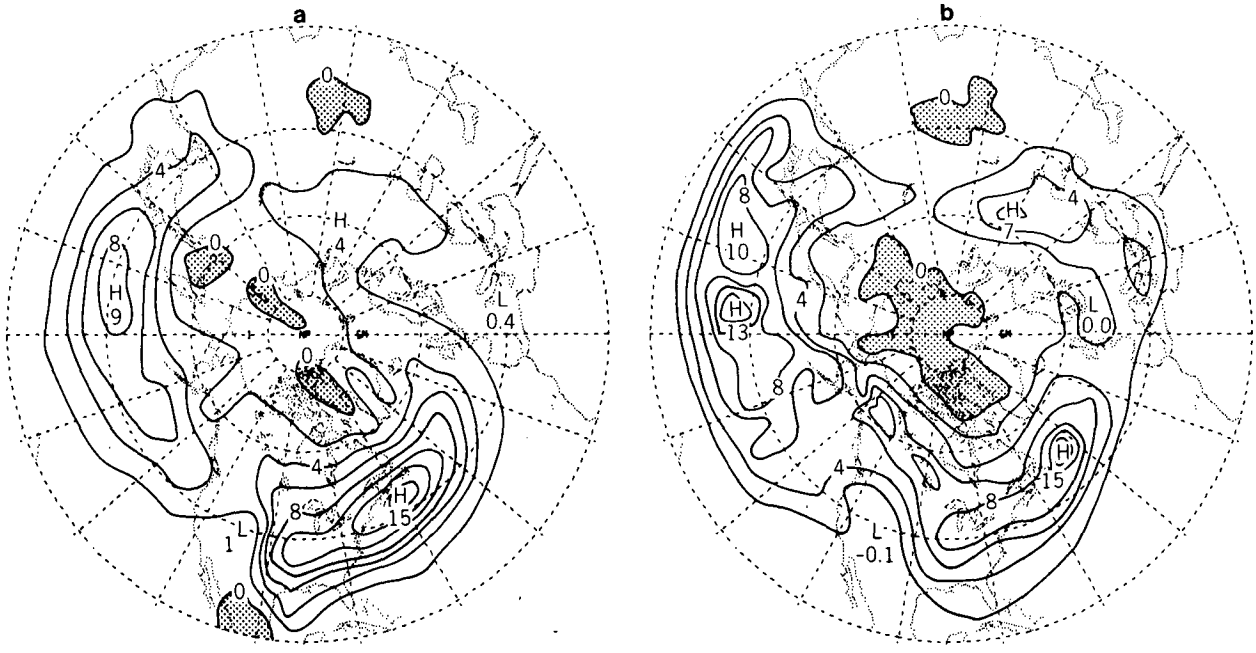

FIG. 14. Distribution of the meridional heat transport by transient eddies, as computed using bandpass filtered data for (a) observations at 850 mb and (b) model simulation at 835 mb. Contour interval 2°C m s^{-1}.

model may be regarded as a dissipative mechanism in the energy balance of these waves.

The distribution of the vertical transport of heat by transient eddies is given in Fig. 16a for NMC data at 700 mb and in Fig. 16b for GFDL model data at 685 mb. The patterns derived from both data sets

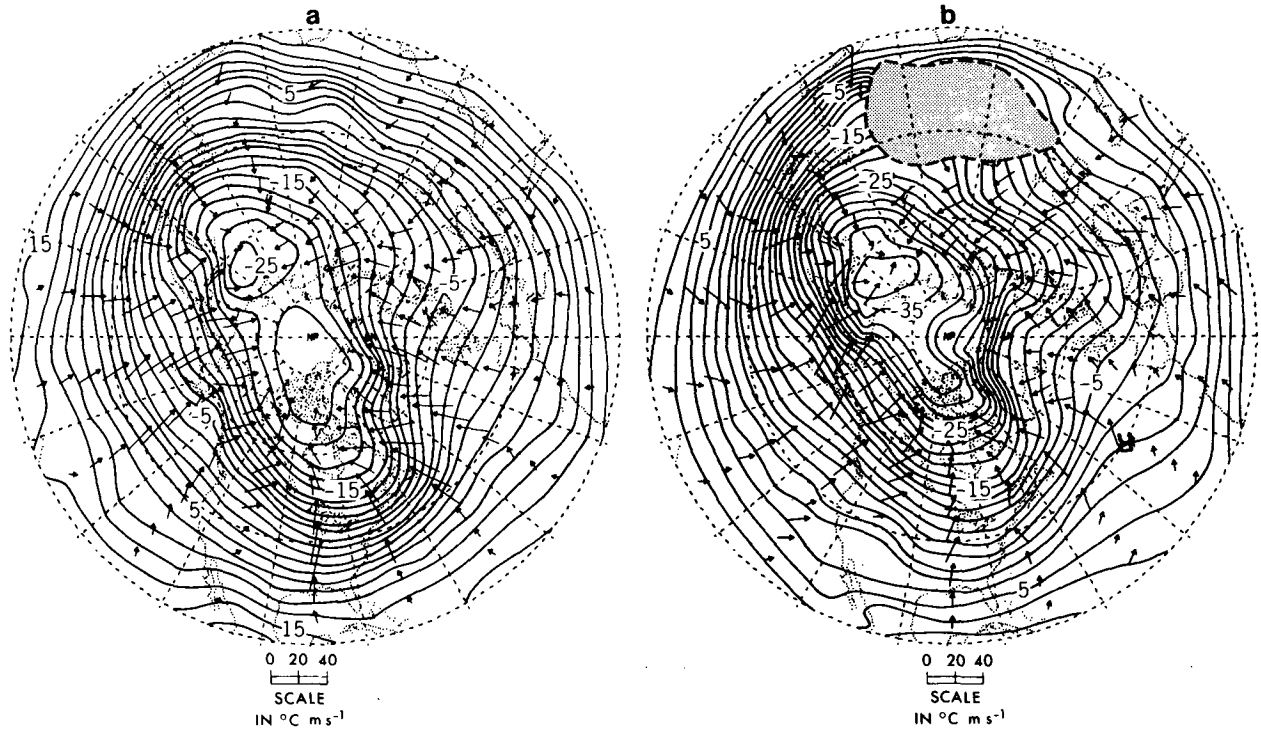

FIG. 15. Vectors show the transient eddy heat flux for (a) observations at 850 mb and (b) model simulation at 835 mb. The length scale for the vectors is given at the lower left-hand corner of the figure. Contours show the time-mean temperature field at the corresponding level; contour interval 2°C.

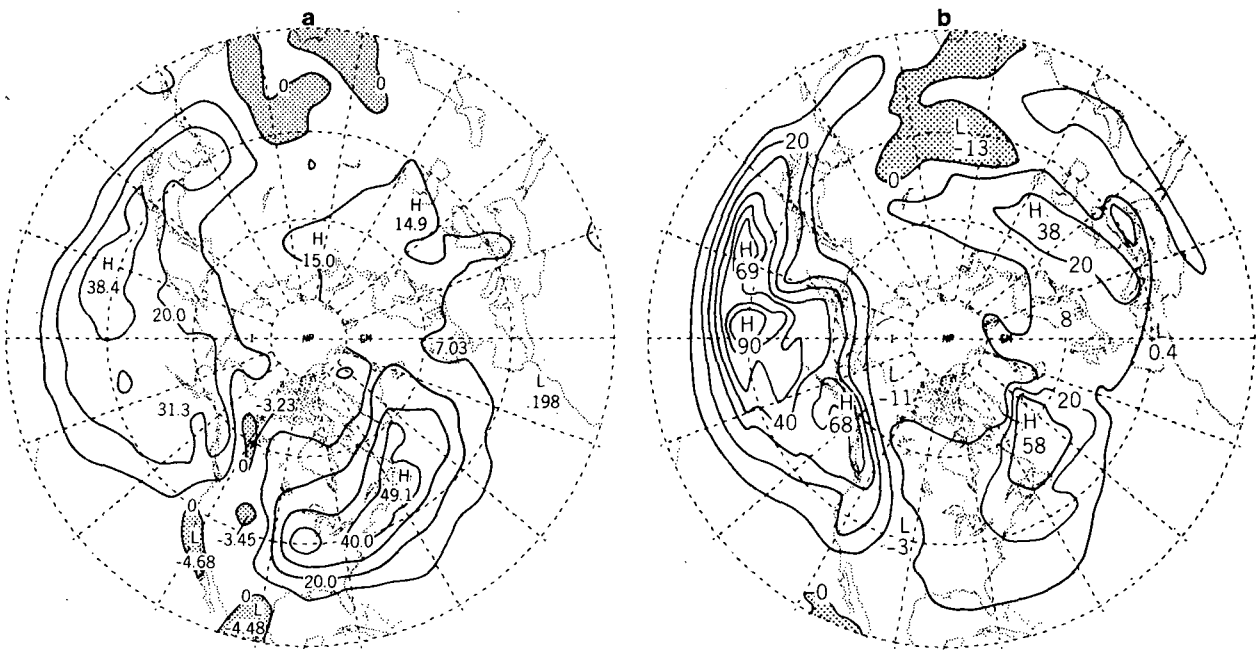

FIG. 16. Distribution of the vertical heat transport by transient eddies, as computed using (a) NMC data at 700 mb and (b) GFDL model data at 685 mb. Contour interval 1×10^{-3} °C mb s^{-1}.

indicate that the principal oceanic storm tracks are characterized by positive temporal correlations between the vertical motion and temperature fields. Such correlations are seen to be much reduced over the western portion of the major continents.

The covariance statistics presented in this subsection suggest that the transient disturbances appearing in both the atmosphere and the model are characterized by well-defined life cycles. The cyclonic shear zones poleward of the wintertime jet streams (Fig. 1) over the western oceans are favored sites for cyclogenesis. As the disturbances begin to travel eastward along the oceanic storm tracks, they extract energy from the mean flow by transporting heat poleward (Figs. 14 and 15) and upward (Fig. 16). As these disturbances reach the western portion of the major land masses, they eventually acquire a more barotropic structure with much weakened heat transports. This interpretation is consistent with the pattern of correlation coefficients between 1000 and 500 mb heights using bandpass filtered data (not shown). The values of the correlation coefficients increase from 0.3–0.4 over the storm tracks to 0.6–0.7 along the west coasts of the major continents.

b. *Momentum transport*

The distribution of the meridional transport of westerly momentum by transient eddies, as computed using bandpass filtered data, is displayed in Fig. 17 for (a) the atmosphere at 300 mb and (b) the GFDL model atmosphere at 315 mb. The model is seen to reproduce the dipole-like structures over the midlatitude oceans, with poleward fluxes to the south of the storm track axes, and equatorward fluxes to the north of them. The intensity of momentum transports in the model is relatively weaker. There is little evidence in the model result of the observed maximum in poleward momentum transport over the western United States.

c. *Potential vorticity transport*

In this study the Ertel potential vorticity in the lower stratosphere is approximated by

$$P \equiv -(\zeta + f)\frac{\partial \theta}{\partial p},$$

where ζ is the relative vorticity defined on constant pressure surfaces, f the Coriolis parameter, θ potential temperature and p pressure. These are adequate approximations for large-scale flows in a hydrostatic and highly stratified atmosphere (e.g., see Hartmann, 1977). It was noted in Lau and Wallace (1979, Fig. 11b) that the transport of potential vorticity by transient eddies near the tropopause tends to converge into regions lying over surface cyclones. This finding was examined in the light of the local balance of potential vorticity for an atmospheric column. In the semi-permanent lows over the northern oceans, the frictional drag associated with the prevalent counterclockwise circulations tend to spin down cyclonic vorticity in the atmos-

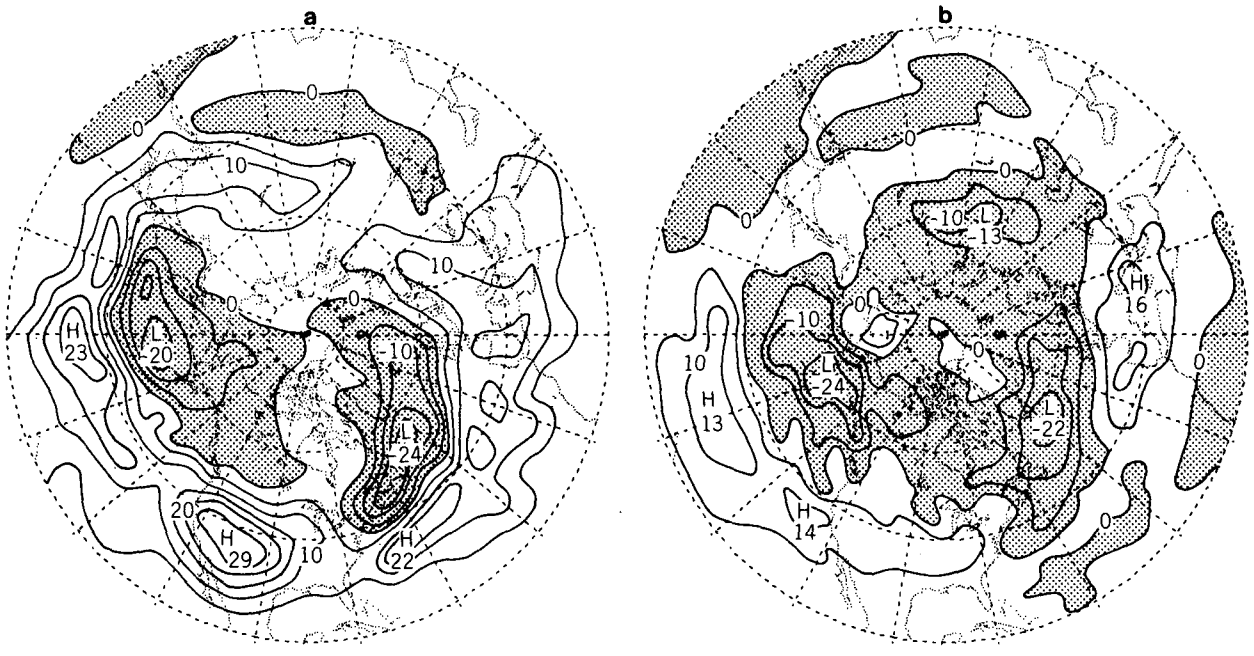

FIG. 17. Distribution of the meridional transport of westerly momentum by transient eddies, as computed using bandpass filtered data for (a) observations at 300 mb and (b) model simulation at 315 mb. Contour interval 5 $m^2 s^{-2}$.

phere; the strong input of heat from the ocean surface and latent heat release also result in destruction of static stability over these regions. The opposite processes, i.e., generation of positive relative vorticity due to the cyclonic frictional torque on the atmosphere, and enhancement of static stability due to cooling from below, act to produce potential vorticity over the surface anticyclones. The time-averaged surface cyclones and anticyclones may hence be regarded as sinks and sources, respectively, of potential vorticity in the atmosphere; and the observed eddy transports from source to sink regions are therefore seen to be in the proper sense to fulfill the balance requirement for potential vorticity.

It would be interesting to examine whether the potential vorticity transport by the eddies appearing in the GCM bears a similiar relationship to the corresponding sea level pressure field. In order to enhance the convergence and divergence features of the potential vorticity fluxes, we shall confine our attention to the irrotational part of the eddy transport, which may be obtained by performing a Helmholtz-type decomposition of the total eddy transport in the manner described in Lau and Wallace (1979, Section 1).[2] The arrows in Fig. 18 depict the vectorial distribution of the irrotational potential vorticity transport for (a) the atmosphere at 200 mb and (b) the model at 190 mb. The contours in these figures represent the corresponding distributions of the sea level pressure field. It is seen that the potential vorticity transport by transient eddies in the model (Fig. 18b) are convergent over the Aleutian low. The pattern over the Icelandic low is less coherent, but the fluxes are generally convergent along the zonal belt between 55 and 60°N over the northern Atlantic. The qualitative agreement between the patterns in Figs. 18a and 18b further substantiates the interpretation of the pattern of eddy potential vorticity transports noted above. It is also worth noting that the magnitudes of potential vorticity transports by the transient eddies in the model are relatively weaker.

7. Conclusions and discussions

In this study, we have examined the hemispheric distributions of a selected set of temporal mean, variance and covariance statistics simulated by a GCM developed in the Geophysical Fluid Dynamics

[2] The vector field of horizontal eddy transport of potential vorticity $\mathbf{F}(P) \equiv \overline{u'P'}\mathbf{i} + \overline{v'P'}\mathbf{j}$ is decomposed into nondivergent and irrotational parts:

$$\mathbf{F}(P) = \mathbf{F}_\psi(P) + \mathbf{F}_\chi(P),$$

where

$$\mathbf{F}_\psi(P) = \mathbf{k} \times \nabla\psi(P),$$

$$\mathbf{F}_\chi(P) = \nabla\chi(P).$$

The flux streamfunction $\psi(P)$ and flux potential function $\chi(P)$ are obtained by solving the Poisson's equations

$$\nabla^2\psi(P) = \mathbf{k}\cdot\nabla \times \mathbf{F}(P),$$

$$\nabla^2\chi(P) = \nabla\cdot\mathbf{F}(P),$$

with the boundary conditions $\psi(P) = 0$, $\chi(P) = 0$ at 20°N.

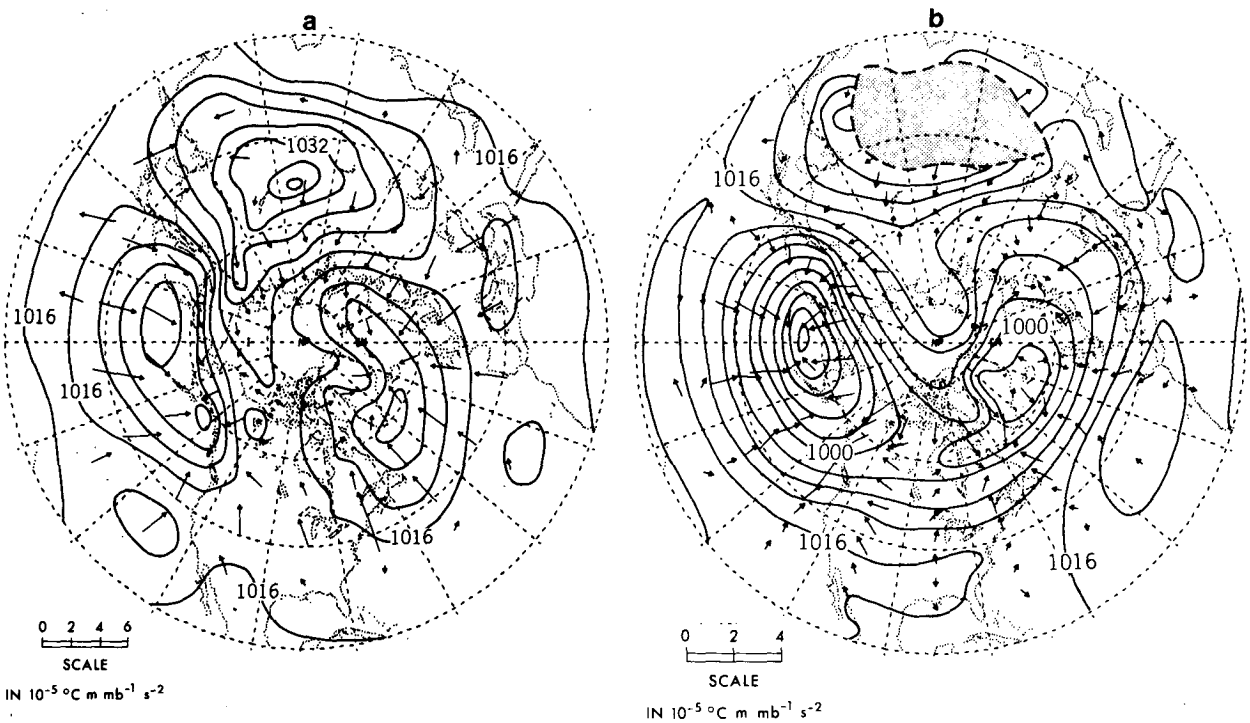

FIG. 18. Vectors show the irrotational transient eddy flux of Ertel potential vorticity for (a) observations at 200 mb and (b) model simulation at 190 mb. The length scale for the vectors is given at the lower left-hand corner of the figure. Contours show the corresponding time-mean sea level pressure field; contour interval 4 mb.

Laboratory. By comparing these model results with the corresponding observed patterns, we have evaluated the ability of this GCM to reproduce the essential regional characteristics of the wintertime circulation. In agreement with observations, the intensity of synoptic-scale fluctuations in the model is enhanced over the oceanic storm tracks, which lie downstream and slightly poleward of the time-averaged jet streams. The vertical profiles of the amplitude of the disturbances appearing in the model-simulated and observed storm tracks are qualitatively similar, although the disturbances in the model are relatively weaker at the higher levels. The vertical structures of geopotential height fluctuations appearing in the atmosphere and the model exhibit very similar geographical variations. The transient disturbances over the oceanic storm tracks are characterized by strong poleward and upward heat transports in the lower troposphere, and by strong convergence of meridional momentum fluxes in the upper levels. The contrast between these baroclinically active regions and the western portions of continents, which are the favored sites for decaying disturbances, is evident in the model results. The observed tendency for the transient eddies to transport heat down the local time-averaged gradient in the lower troposphere, and to transport potential vorticity near the tropopause from source to sink regions also shows up in the model simulation.

In conjunction with this comparative study, a parallel set of circulation statistics has also been compiled from the simulation of a second generation GCM developed at the National Center for Atmospheric Research (NCAR). This particular model version uses geometric heights as the vertical coordinate. There are six layers with a uniform height increment of 3 km. The effective horizontal resolution is comparable to that of the GFDL model. Other details of the model formulation are described by Kasahara *et al.* (1973). While it is not our intention to offer a lengthy assessment of the NCAR simulation, the following aspects of the model performance are worth noting:

1) The amplitudes of the transient low-pass and bandpass fluctuations at 500 mb in the NCAR model are weaker than the corresponding values for both observations and the GFDL model.

2) The geographical location and intensity of the North American jet stream, as well as the location of the Atlantic storm track, are reproduced by the NCAR simulation. However, the axis of the stationary trough over the western Pacific and the associated Asian jet stream are displaced eastward relative to their observed positions by ~30° of longitude. The axis of the Pacific storm track at 500 mb is shifted poleward and extends all the way across Alaska.

3) Contrary to observations, the amplitudes of the

bandpass fluctuations in the NCAR model decrease monotonically with height between sea level and the 9 km level. This feature is also evident in the study of Pratt (1979, Figs. 8 and 9), who has compared the space-time spectra for both the NCAR and GFDL models[3] with observations.

4) The Icelandic and Aleutian lows in the NCAR simulation of the time-averaged sea level pressure field are characterized by relatively limited spatial extents; the presence of several high pressure centers over the North American continent leads to an anomalous easterly circulation over the southern United States.

For both the NCAR and GFDL simulations, the correspondence between the low-frequency, planetary-scale phenomena in the models and those in the atmosphere is poorer than the correspondence for the bandpass fluctuations. Although the inadequate sampling of such slowly varying phenomena over the relatively limited duration of the model runs may partially account for this behavior, it is most likely that the simulation errors at large scales and low frequencies are manifestations of certain basic deficiencies in the current generation of GCM's.

In order to put the difference between the observed and simulated statistics in a proper perspective, it is worth noting that, despite the efforts made during the past decades to improve the data coverage of the Northern Hemisphere, large areas over the oceans are still devoid of regular rawinsonde observations. In the twice-daily NMC operational forecast/analysis cycle, the interpolation over these data-sparse regions is achieved by using the 12 h numerical forecast as a first-guess field, which ensures that the known dynamical constraints such as hydrostatic and gradient wind balances are applied to the gridded data on a routine basis. The data-processing system also incorporates information from sources other than radiosondes, such as reports from mobile ships and aircraft, and cloud-wind vectors derived from satellite imagery. While the fidelity of the NMC data set has yet to be demonstrated by comparison with circulation statistics based on more elaborate observing and analysis techniques (such as those implemented in the Global Weather Experiment), we believe that the basic conclusions of the present study are not substantially affected by the uncertainties of the observational data over the oceans.

Acknowledgments. We would like to thank Prof. J. M. Wallace and Dr. Y. Hayashi for their continued interest in this study, Drs. I. Held, E. O. Holopainen, J. D. Mahlman, S. Manabe and A. M. Oort for offering constructive comments on the manuscript, and Mr. D. G. Golder for his assistance in extracting the data from the GCM history tapes. This work was initiated when one of us (NCL) was associated with the University of Washington through the support of National Science Foundation Grant ATM 78-07369 (Climate Dynamics Program, Climate Dynamics Research Section, Division of Atmospheric Sciences) and an NCAR Graduate Assistant. The work was completed when NCL was a Visiting Scientist in the Geophysical Fluid Dynamics Program, which was supported by NOAA Grant 04-7-022-44017. Acknowledgment is also made to Messrs. John Conner, William Ellis and Philip Tunison of the Geophysical Fluid Dynamics Laboratory for their assistance in drafting the figures.

[3] The NCAR model analyzed in Pratt's work has approximately half the resolution of the version described here. The same GFDL model provided the data for this and Pratt's studies.

REFERENCES

Arakawa, A., 1972: Design of the UCLA general circulation model. Tech. Rep. 7, Dept. of Meteorology, University of California, Los Angeles, 116 pp. [Available from UCLA Dept. of Meteorology, 405 Hilgard Ave., Los Angeles 90024.]

Blackmon, M. L., 1976: A climatological spectral study of the 500 mb geopotential height of the Northern Hemisphere. *J. Atmos. Sci.*, **33**, 1607–1623.

——, J. M. Wallace, N.-C. Lau and S. L. Mullen, 1977: An observational study of the Northern Hemisphere wintertime circulation. *J. Atmos. Sci.*, **34**, 1040–1053.

——, R. A. Madden, J. M. Wallace and D. S. Gutzler, 1979: Geogaphical variations in the vertical structure of geopotential height fluctuations. *J. Atmos. Sci.*, **36**, 2450–2466.

Chervin, R. M., W. M. Washington and S. H. Schneider, 1976: Testing the statistical significance of the response of the NCAR general circulation model and North Pacific ocean surface temperature anomalies. *J. Atmos. Sci.*, **33**, 413–423.

Gates, W. L., 1975: The January global climate simulated by a two-level general circulation model: a comparison with observations. *J. Atmos. Sci.*, **32**, 449–477.

Hahn, D. G., and S. Manabe, 1975: The role of mountains in the South Asian monsoon circulation. *J. Atmos. Sci.*, **32**, 1515–1541.

Hartmann, D. L., 1977: On potential vorticity and transport in the stratosphere. *J. Atmos. Sci.*, **34**, 968–977.

Hayashi, Y., 1974: Spectral analysis of tropical disturbances appearing in a GFDL general circulation model. *J. Atmos. Sci.*, **31**, 180–218.

——, and D. G. Golder, 1977: Space-time spectral analysis of mid-latitude disturbances appearing in a GFDL general circulation model. *J. Atmos. Sci.*, **34**, 237–260.

Kasahara, A., and W. M. Washington, 1971: General circulation experiments with a six-layer NCAR model, including orography, cloudiness, and surface temperature calculations. *J. Atmos. Sci.*, **28**, 657–701.

——, T. Sasamori and W. M. Washington, 1973: Simulated experiments with a 12-layer stratospheric global circulation model. I. Dynamical effect of the earth's orography and thermal influence of continentality. *J. Atmos. Sci.*, **30**, 1229–1251.

Kurihara, Y., and J. L. Holloway, Jr., 1967: Numerical integration of a nine-level global primitive equation model formulated by the box method. *Mon. Wea. Rev.*, **95**, 509–530.

Lau, N.-C., 1978: On the three-dimensional structure of the observed transient eddy statistics of the Northern Hemisphere wintertime circulation. *J. Atmos. Sci.*, **35**, 1900–1923.

——, 1979a: On the structure and energetics of transient disturbances in the Northern Hemisphere wintertime circulation. *J. Atmos. Sci.*, **36**, 982–995.

——, 1979b: The observed structure of tropospheric stationary waves and the local balances of vorticity and heat. *J. Atmos. Sci.*, **36**, 996–1016.

——, and J. M. Wallace, 1979: On the distribution of horizontal transports by transient eddies in the Northern Hemisphere wintertime circulation. *J. Atmos. Sci.*, **36**, 1844–1861.

Manabe, S., 1969: Climate and ocean circulation: I. The atmosphere and the hydrology of the earth's surface. *Mon. Wea. Rev.*, **97**, 739–774.

——, and R. T. Wetherald, 1967: Thermal equilibrium of the atmosphere with a given distribution of relative humidity. *J. Atmos. Sci.*, **24**, 241–259.

——, and T. B. Terpstra, 1974: The effects of moutains on the general circulation of the atmosphere as identified by numerical experiments. *J. Atmos. Sci.*, **31**, 3–42.

——, and J. L. Holloway, Jr., 1975: The seasonal variation of the hydrologic cycle as simulated by a global model of the atmosphere. *J. Geophys. Res.*, **80**, 1617–1649.

——, and R. T. Wetherald, 1975: The effects of doubling of the CO_2 concentration on the climate of a general circulation model. *J. Atmos. Sci.*, **32**, 3–15.

——, J. Smagorinsky and R. F. Strickler, 1965: Simulated climatology of a general circulation model with a hydrologic cycle. *Mon. Wea. Rev.*, **93**, 769–798.

——, D. G. Hahn, and J. L. Holloway, Jr., 1974: The seasonal variation of the tropical circulation as simulated by a global model of the atmosphere. *J. Atmos. Sci.*, **31**, 43–83.

Pratt, R. W., 1979: A space-time spectral comparison of the NCAR and GFDL general circulation models of the atmosphere. *J. Atmos. Sci.*, **36**, 1681–1691.

Somerville, R. C. J., P. H. Stone, M. Halem, J. E. Hansen, J. S. Hogan, L. M. Druyan, G. Russel, A. A. Lacis, W. J. Quirk and J. Tenenbaum, 1974: The GISS model of the global atmosphere. *J. Atmos. Sci.*, **31**, 84–117.